

See discussions, stats, and author profiles for this publication at: <https://www.researchgate.net/publication/262014397>

Substrate Dependent Water Splitting with Ultrathin $\alpha\text{-Fe}_2\text{O}_3$ Electrodes

DATASET in THE JOURNAL OF PHYSICAL CHEMISTRY C · APRIL 2014

Impact Factor: 4.77

CITATIONS

2

READS

25

3 AUTHORS, INCLUDING:



Omid Zandi

University of Texas at Austin

14 PUBLICATIONS 221 CITATIONS

SEE PROFILE



Thomas William Hamann

Michigan State University

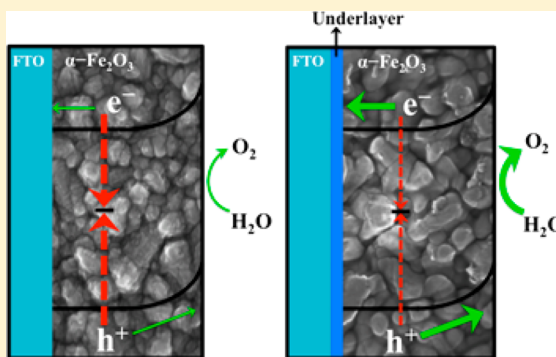
52 PUBLICATIONS 2,203 CITATIONS

SEE PROFILE

Substrate Dependent Water Splitting with Ultrathin α -Fe₂O₃ Electrodes

Omid Zandi,[†] Joseph A. Beardslee,[‡] and Thomas Hamann^{*,†}[†]Department of Chemistry, Michigan State University, East Lansing, Michigan 48824-1322, United States[‡]Division of Chemistry and Chemical Engineering, California Institute of Technology, Pasadena, California 91125, United States**S** Supporting Information

ABSTRACT: Thin films of hematite (α -Fe₂O₃) were deposited by atomic layer deposition (ALD), and the effects of metal oxide underlayers on the photocatalytic water oxidation performance were investigated. It was found that a Ga₂O₃ underlayer dramatically enhances the water oxidation performance of the thinnest hematite films. The performance enhancement is attributed to the increased crystallinity of the ultrathin films induced by the oxide underlayers. The degree of crystallinity was examined by Raman line shape analysis of the characteristic hematite phonon modes. It was found that multiple metal oxide underlayers, including Nb₂O₅, ITO, and WO₃, increase the film crystallinity compared to hematite deposited on bare FTO. The increased crystallite size was also clearly evident from the high resolution SEM images. The degree of crystallinity was found to correlate with absorbance and the photocatalytic water oxidation performance. These findings shed light on the origin of the dead layer at the interface of the FTO substrate and ultrathin hematite films and elucidate strategies at overcoming it.

**■ INTRODUCTION**

Solar water splitting in photoelectrochemical (PEC) cells is a type of energy conversion scheme that converts sunlight into the chemical fuel H₂.^{1–3} This scheme is particularly attractive since the combination of sunlight and water provide essentially unlimited resources to produce renewable, carbon neutral and widely available fuels. In a PEC cell, a semiconductor electrode is responsible for the absorption of sunlight and transport of the resultant charge carriers to their respective contacts, while the interface between the semiconductor (photoanode) and the liquid electrolyte plays the key role in the subsequent chemical reactions.^{1,2,4,5} For a single semiconductor to achieve efficient water oxidation, a combination of several material requirements must be met: absorption of a sufficient portion of the solar spectrum, band edge positions capable of oxidizing H₂O, electrode stability in aqueous electrolytes over a range of pH conditions, and composition of earth abundant elements. Primarily due to their stability in aqueous media, metal oxide semiconductors have been the premier focus for carrying out the H₂O oxidation half reaction of solar water splitting.^{6,7} Among different metal oxides studied for this purpose,^{7,8} hematite (α -Fe₂O₃) comprises the most promising properties for PEC water oxidation.^{2,7–12} Its 2.1 eV band gap absorbs a good fraction of the solar spectrum, up to \sim 580 nm. In addition to good light absorption, hematite is stable in contact with neutral and basic aqueous electrolytes and possesses a very positive valence band edge suitable for H₂O oxidation (\sim 2.7 V vs RHE).⁴ Further, iron and oxygen are two of the most abundant elements in the earth's crust. Despite these favorable

characteristics, the overall solar energy conversion efficiency with hematite electrodes has been poor.^{9,10,13}

The efficiency of solar-driven water oxidation on a semiconductor photoanode is determined by three major processes: the light harvesting efficiency (LHE), the efficiency of the photogenerated holes reaching the solution interface (hole transport efficiency), and hole collection efficiency via water oxidation at the electrode surface (water oxidation efficiency). The majority of photogenerated holes in the bulk of the semiconductor undergo recombination resulting in a negligible diffusion length. The electric field that develops in the depletion region is capable of driving holes to the electrolyte interface; however, the depletion width is only \sim 20 nm.¹⁴ Thus, the very short minority charge collection length (\sim 10 nm) combined with the relatively long visible light absorption depth (hundreds of nanometers) prevents the realization of both a high LHE and hole transport efficiency.^{10,12,14,15} This limitation has been partially circumvented by deconvoluting the light absorption from hole transport directions with nanostructured electrodes.^{12,16–18} Nanostructured electrodes have been shown to produce significantly higher water oxidation photocurrents by minimizing the distance that holes should travel to be collected without

Special Issue: Michael Grätzel Festschrift**Received:** November 27, 2013**Revised:** April 22, 2014

sacrificing LHE. The first really successful example of this strategy was the seminal report by Grätzel and co-workers who prepared nanocauliflower hematite photoelectrodes via chemical vapor deposition which resulted in current densities in excess of 3 mA cm^{-2} at 1.23 V vs RHE .^{12,19} An alternative approach, first demonstrated by Grätzel and co-workers, is to use a host–guest motif where thin films of hematite are deposited on a high aspect ratio substrates.^{20,21} This approach was extended by Wang and co-workers who employed atomic layer deposition (ALD) to deposit conformal hematite thin films on TiSi_2 nanonet scaffolds.¹⁶ We have shown, however, that even optimized thin film electrodes have absorbed photon to current efficiencies (APCE) less than unity.^{10,14} It is therefore crucial to understand what factors limit the performance of ultrathin ($<20 \text{ nm}$) hematite films.

Depletion region and surface state electron–hole recombination are known to be factors which limit the APCE of hematite electrodes.^{10,22} The hole collection efficiency via H_2O oxidation reaction at the hematite–water interface has recently been studied in detail.^{4,5,23–26} It was found that the four-hole water oxidation reaction is in competition with surface state recombination, limiting the hole collection efficiency. Efforts toward improving the water oxidation efficiency have consisted of adding surface coatings, aiming to suppress surface recombination or catalytically enhance the water oxidation reaction.^{19,27–29} Another strategy employed to increase the hole transport efficiency is bulk modification by elemental doping. Doping hematite can in principle increase the lifetime and/or mobility of photogenerated holes and thus increases the hole transport efficiency.^{30,31} Numerous examples of enhanced water oxidation performance with hematite electrodes upon doping with dopants e.g. Ti, Si, Sn, Al, Cr, Pt, Nb, Mg, and Ge have been reported.^{31–41} We recently studied the effect of Ti doping on water oxidation performance of hematite electrodes; it was found that the effect of Ti dopants is significantly higher for the thinnest electrodes ($\sim 20 \text{ nm}$), with minor effect on thicker electrodes. We suggested that the effect of Ti doping is actually to activate the so-called dead layer at the substrate–hematite back contact thus increasing the hole transport efficiency.³¹

While the exact cause of the dead layer is still not fully understood, some combination of an accelerated rate of recombination and/or decreased hole mobility in the dead layer prevents the efficient charge separation and transport to the electrolyte interface to perform the subsequent water oxidation reaction.^{31,42} Itoh and Bockris reported the thickness dependent photoelectrochemical behavior of hematite electrodes prepared by spray pyrolysis.^{11,43} They observed negligible photocurrent for water oxidation with 20 nm electrodes. They attributed this to the fact that in the sufficiently thin films, the diffusion length for electrons from the SnO_2 layer extends into the hematite film, causing enhanced recombination.⁴³ Liang et al. attributed the poor water oxidation efficiency with hematite to the enhanced recombination at the trap states in the substrate–hematite interface.⁴⁴ Souza et al. studied the influence of the film thickness on water oxidation on nanostructured hematite films prepared by spin coating and found that the photocurrent increases with increasing thickness from 25 to 165 nm , with negligible currents for 25 nm electrodes.⁴⁵ Significantly lower photocurrent for thinner electrode was attributed to the enhanced electron–hole recombination at the intermediate states close to the conduction band as a result of stress induced by the interaction

of the film and the substrate.⁴⁵ Le Formal et al. attributed the dead layer effect to the lack of crystallinity and enhanced recombination sites at the hematite–substrate interface.⁴² Sivula, Grätzel, and co-workers studied the PEC water oxidation on ultrathin hematite electrode prepared by APCVD and spray pyrolysis.^{33,42} They attributed the significantly lower photoactivity for thinnest films to an increased recombination rate at the FTO–hematite interface due to the formation of the dead layer.⁴²

Efforts to mitigate the dead layer effect have primarily consisted of modifying the transparent conductive substrate with oxide underlayers. Incorporation of a 5 nm SnO_2 underlayer, or Si doping, was shown to enhance the photocatalytic water oxidation efficiency.⁴⁴ A similar effect was also demonstrated with a monolayer of SiO_2 .⁴² Subsequently Hisatomi et al. studied the water oxidation with ultrathin hematite films prepared by spray pyrolysis and suggested that the strain induced by a lattice mismatch can be mitigated by a Ga_2O_3 underlayer.⁴⁶ In a subsequent report, similar effects were observed for ultrathin hematite films with 2 nm of Nb_2O_5 or TiO_2 underlayers.⁴⁷ The effect of these oxide underlayers was attributed to suppressed electron back-recombination from the FTO to the hematite thin film.

Although significant improvement in the water oxidation efficiency with hematite ultrathin films has been achieved by the incorporation of oxide underlayers, the specific physical effect of oxide underlayers has not been unambiguously determined. This work is aimed at acquiring a clearer picture of the cause of the dead layer as well as the effects of underlayers. We present a thorough investigation of PEC water oxidation with hematite thin films with and without Ga_2O_3 underlayer. We utilize the advantages of atomic layer deposition, ALD, to synthesize thin films of hematite electrodes with controlled geometry and composition. Ultrathin films of hematite prepared via ALD are pinhole free, enabling the uniform and conformal coverage of the underlying substrate. Uniformity and simple geometry of these planar thin films, therefore, serve as excellent model systems to probe the effect of the oxide underlayers. We further compare the PEC behavior of the hematite electrodes of different thicknesses with and without a variety of metal oxide underlayers with that of Ti-doped analogues under water oxidation conditions. A combination of photoelectrochemical, spectroscopic, and microscopic measurement allowed us to clearly determine the physical causes of improved PEC behavior through incorporation of the oxide underlayer and shed light the origin of the dead layer.

■ EXPERIMENTAL SECTION

Electrode Preparation. Thin films of Fe_2O_3 were deposited on fluorine-doped tin oxide (FTO)-coated glass substrates (Hartford Glass, $15 \Omega \text{ cm}^{-2}$) by atomic layer deposition, ALD (Savannah 100, Cambridge Nanotech Inc.), using the procedure described previously.^{4,14,31} Briefly, the FTO glass was cleaned by sequential sonication in soap, water, and isopropyl alcohol. Fe_2O_3 was deposited onto the cleaned FTO substrate by alternating pulses of ferrocene as iron precursor and a combination of water and ozone as oxidant. The ferrocene cylinder, heated to 70°C , was pulsed for 20 s and was followed by an oxidation cycle which included 10 subcycles of a $0.015 \text{ s H}_2\text{O}$ pulse followed by a 2 s ozone pulse, where each subcycle was separated by a 5 s purge. During all depositions, Fe_2O_3 was also grown on control Si substrates to determine the film thickness through spectroscopic ellipsom-

etry measurements (Horiba Jobin Yvon, Smart-SE). The film thicknesses were determined over the wavelength region 800–1000 nm, where all the oxides are transparent, to allow for accurate results, independent of any variation of extinction. Additional Si substrates were coated with 70 nm of SnO_2 prior to the deposition of Fe_2O_3 to determine the influence of the FTO substrate on the growth rate; fit results remained within the margin of error of films deposited directly on Si substrates. Ga_2O_3 was deposited on FTO by ALD using tris-(dimethylamido)gallium(III) ($\text{Ga}_2(\text{NMe}_2)_6$) (Strem Chemicals Inc.) as Ga precursor and H_2O as oxidant using a modified version of previously reported procedure.⁴⁸ For the Ga_2O_3 deposition, the precursor cylinder was heated to 150 °C and pulsed for 0.2 s under exposure mode for 8 s, followed by 12 s purge. Then a 0.015 s pulse of H_2O was introduced under the same exposure-purge time to oxidize the Ga precursor. A growth rate of 1.1 Å Ga_2O_3 /cycle was measured by ellipsometry on control Si wafers. Ga_2O_3 coated FTO substrates were subsequently coated with the desired thickness of Fe_2O_3 . After the deposition of Fe_2O_3 , films were annealed by heating to 500 °C at a rate of 17 °C/min, sintered at 500 °C for 30 min, and allowed to cool to room temperature over 2 h. For Ti-doped electrodes, titanium isopropoxide was used as the titanium precursor to add titanium to films using our previously reported procedure.³¹ Nb_2O_5 was deposited on FTO by ALD using Nb(V) ethoxide ($\text{Nb}(\text{OCH}_2\text{CH}_3)_5$) (Sigma-Aldrich) as Nb precursor and H_2O as oxidant. For the Nb_2O_5 deposition, Nb cylinder was heated to 150 °C and pulsed for 0.2 s. After 8 s exposure, the chamber was purged for 12 s. The same exposure/purge time was used for the oxidant, water. The ALD chamber temperature was set at 200 °C for Nb_2O_5 deposition. WO_3 was deposited using bis(*tert*-butylimino)bis-(dimethylamino)tungsten(VI) (Sigma-Aldrich) as precursor and H_2O as oxidant. Briefly, the W cylinder was heated to 75 °C and pulsed for 2 s. After 10 s exposure, the chamber was purged for 10 s. The same exposure/purge time was used for the oxidant, water. The ALD chamber temperature was maintained at 260 °C for WO_3 deposition. SnO_2 was deposited using $\text{Sn}(\text{NMe}_2)_4$ (Sigma-Aldrich) as ALD precursor and ozone as oxidant. The Sn precursor cylinder was heated to 60 °C and pulsed for 0.5 s followed by 10 s purge. A 12 s O_3 pulse was used as an oxidant followed by a 10 s purge. The ALD chamber temperature was maintained at 230 °C for SnO_2 deposition. Indium tin oxide (ITO)-coated glass substrates (SPI supplies, 8–12 $\Omega \text{ cm}^{-2}$) were used as analogues of an ITO underlayer substrate.

Film Characterization. X-ray photoelectron spectroscopy (XPS) was carried out on a Kratos Axis Ultra system with a base pressure of $<1 \times 10^{-9}$ Torr. A monochromated Al $K\alpha$ source was used to illuminate the sample with 1486.7 eV photons at a power of 150 W. A hemispherical analyzer oriented for detection along the sample surface normal was used. Survey scans were obtained at a resolution of 1 eV with a pass energy of 80 eV. Detailed scans were acquired at a resolution of 25 meV with a pass energy of 10 eV using variable acquisition times. For depth profiling studies, an octopole ion gun was used to etch the sample surface with 500 eV Ar ions for 180 s per step.

The surface morphology of the prepared films was examined by scanning electron microscopy, SEM (Carl Zeiss Auriga, Dual Column FIBSEM). Absorbance measurements were made using a PerkinElmer Lambda35 UV–vis spectrometer with a Labsphere integrating sphere. The absorbance spectra of the

films were measured by illuminating from the substrate-electrode interface. The incident light was corrected for passing through and being reflected by the substrate using a previously reported approach.¹⁴ Raman spectroscopy measurements were made LabRam Armis, Horiba Jobin Yvon instrument equipped with 532 nm laser and a microscope to focus the laser light on the film surface.

Photoelectrochemical Measurements. For photoelectrochemical measurements, electrodes were masked with a 60 μm Surllyn film (Solaronix) with a 0.28 cm^2 hole to define the active area and to prevent scratching of the thin films. Surllyn films were adhered to the electrodes by heating to 115 °C. The electrodes were examined in contact with aqueous solutions buffered to pH 6.9 using a 0.1 M phosphate buffer, with 200 mM KCl as a supporting electrolyte. A homemade saturated Ag/AgCl electrode was used as a reference electrode, and a high surface area platinum mesh was used as the counter electrode. The reference electrode was regularly calibrated vs saturated calomel electrode (SCE) (Koslow Scientific), and all potentials were converted to the reversible hydrogen electrode (RHE) scale by the equation $V_{\text{RHE}} = V_{\text{Ag/AgCl}} + 0.197 \text{ V} + \text{pH}$ (0.059 V). Photoelectrochemical measurements were made with an Eco Chemie Autolab potentiostat coupled with Nova electrochemical software. For the current–potential measurements, potential was cycled linearly between 0.0 and 1.6 V vs Ag/AgCl at the rate of 20 mV s^{-1} . The light source was a 450 W Xe arc lamp (Horiba Jobin Yvon). An AM 1.5 solar filter was used to simulate sunlight at 100 mW cm^{-2} (1 sun). Unless otherwise stated, all photoelectrochemical tests were carried out by shining light on the electrodes through the FTO substrate (back illumination). For back illumination electrodes were clamped to a custom-made glass electrochemical cell. For the front side illumination (electrolyte side) a homemade cell with high optical quality quartz window was used.

■ RESULTS AND DISCUSSION

Hematite films prepared from 300 ALD cycles were deposited on bare FTO substrates ($18.9 \pm 0.03 \text{ nm}$) and FTO substrates coated with a 2 nm Ga_2O_3 underlayer ($18.1 \pm 0.02 \text{ nm}$). Current density, J , vs applied voltage, V , curves of the ~18 nm thick hematite electrodes with and without a Ga_2O_3 underlayer are shown in Figure 1. We note that the 18.9 nm hematite electrodes deposited on FTO showed negligible photocurrent due to the severe effect of the dead layer on this substrate, consistent with previous reports.^{42,47} The dramatic shift in the photocurrent onset potential along with a much higher photocurrent indicates the superior photocatalytic activity of the Ga_2O_3 modified film compared to the unmodified electrodes in accord with the previous report.⁴⁶

We recently studied the effect of Ti doping on the PEC water oxidation performance of hematite electrodes.³¹ It was found that performance improvement upon Ti doping is greatest for the thinnest electrodes. We suggested that the Ti activates the dead layer by facilitating charge separation most possibly by increasing the film crystallinity. The effect of a Ga_2O_3 underlayer on Ti-doped electrodes of the same thickness is shown in Figure 1b. As it can be seen the incorporation of the underlayer has a negligible effect on the water oxidation performance of Ti-doped electrodes, indicating the dead layer already being eliminated by Ti doping. In other words, Ti doping does not further improve the performance of Ga_2O_3 modified electrodes. Since Ti-doped thin films as well as thicker hematite films, as discussed in detail below, were well-behaved

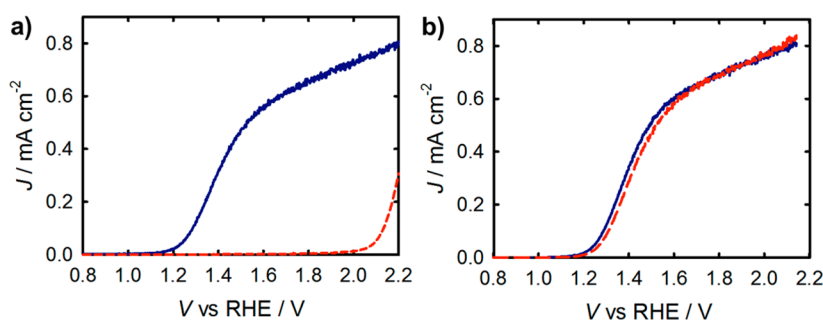


Figure 1. a) J – V curves of ~ 18 nm thick hematite electrodes with (solid dark blue) and without (dashed red) a 2 nm Ga_2O_3 underlayer in response to 1 sun illumination. Dark J – V curves are provided in the SI. b) J – V curves of ~ 18 nm thick Ti-doped hematite electrodes with (solid dark blue) and without (dashed red) a 2 nm Ga_2O_3 underlayer.

when deposited on the same FTO substrates, a trivial cause of the poor performance of defective (e.g., nonconductive) substrates can be ruled out.

A Ga_2O_3 underlayer can improve the PEC water oxidation with hematite in several different ways. Cesar et al.³³ as well as Itoh and Bockris^{11,43} attributed the poor water oxidation performance of hematite thin films to the increased recombination rate at the hematite-FTO interface. They suggested that possible mixing of SnO_2 and Fe_2O_3 at the hematite-FTO interface could induce trap states, enhancing electron–hole recombination at the back contact. In principle a Ga_2O_3 underlayer can block the possible Fe and Sn interdiffusion during film preparation and annealing. Therefore, the performance enhancement can be a result of less significant mixing at the hematite-FTO interface in the presence of a Ga_2O_3 underlayer. In order to control for this possibility, samples of hematite, deposited on Ga_2O_3 modified and bare FTO, were prepared and characterized by XPS depth profiling measurements. The effect of a Ga_2O_3 underlayer should be obvious by comparing films treated at different temperatures, with and without an underlayer. The results of XPS depth profiling are shown in Figure 2. Substantial overlap between the profiles of different atomic concentrations can be seen in every case. Since the escape depth of photoelectrons is on the order of 2–10 nm, part of the overlap can be attributed to the fact

that the signal is composed of surface layers as well as layers of the underlying material. Unfortunately this overlap makes it difficult to accurately determine the extent of elemental diffusion at the hematite/FTO interface. However, a relative comparison can be made of the films deposited on FTO and Si substrates, since no diffusion of Fe or Sn is expected into the Si substrate. For example, by comparing the Fe profile in a hematite film deposited on FTO (Figure 2a) and on SnO_2 coated Si substrate (Figure 2b), substantial mixing of Fe_2O_3 and SnO_2 is evident. For hematite films deposited on SnO_2 coated Si substrates, the Fe profile declines to zero after ~ 30 min sputtering time, while for the same hematite film thickness on FTO, the Fe profile showed nonzero values throughout the underlying FTO layer. Since no Fe was detected in bare FTO substrate, there is apparently substantial mixing Fe and/or Sn at the substrate interface. In the presence of a Ga_2O_3 underlayer, however, nominally identical atomic profiles were observed for Fe, with Fe signals persisting past the Ga signal as shown in Figure 2c. Thus, the improvement in water oxidation performance upon underlayer incorporation cannot be associated with the mitigation of diffusion effect at the back contact by the Ga_2O_3 layer. In other words, the dead layer is clearly not a result of possible mixing of Fe_2O_3 and FTO substrate. This makes sense since the SnO_2 underlayer itself was also reported to improve the water oxidation performance of hematite electrodes.⁴⁴ We note that the mixing at the FTO/hematite interface was also observed by Kronawitter et al. for hematite thin film through soft X-ray absorption measurements.⁴⁹ The interface was found to be associated with a distribution of unoccupied oxygen p-hybridized states located below the conduction band, which are eliminated with high-temperature processing.

In addition, from Figure 2c it can be seen that the Ga profile shows nonzero values over a wide range of sputtering time extended into the Fe_2O_3 and SnO_2 layers. Comparing this profile to that of the same thickness of Ga_2O_3 deposited on Si (Figure 2d), where the Ga concentration declines to zero within 3 min of sputtering, shows that there is substantial Ga diffusion into the adjacent Fe_2O_3 and SnO_2 layers. Therefore, the question arises whether the performance enhancement by the underlayer is simply a consequence of doping hematite with Ga atoms. J – V curves of hematite electrodes having 1, 2, and 4 nm Ga_2O_3 underlayers are shown in Figure 2S which indicate an optimum Ga_2O_3 underlayer thickness of 2 nm, consistent with a previous report.⁴⁸ While an effect from doping is also expected for the 1 and 4 nm Ga_2O_3 underlayers, the water oxidation efficiency was significantly lower with these thicknesses of the underlayer. To further determine the

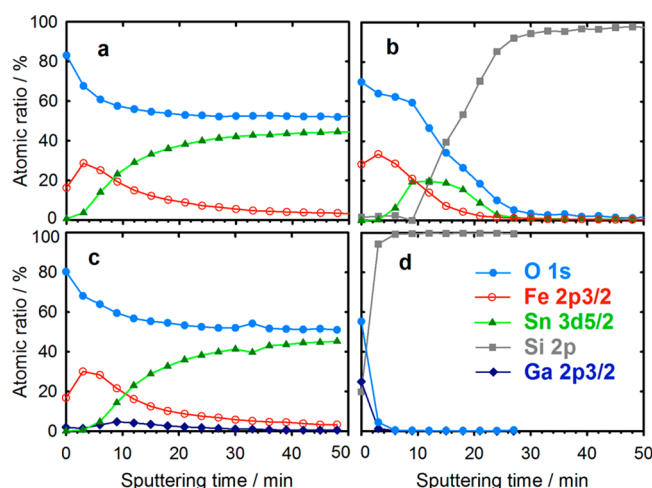


Figure 2. a) XPS depth profile of 18.1 nm Fe_2O_3 deposited on FTO. b) The same thickness of Fe_2O_3 on a SnO_2 coated Si wafer. c) The profile of 18.9 nm Fe_2O_3 with a 2 nm Ga_2O_3 underlayer deposited on FTO. d) The profile of 2 nm Ga_2O_3 deposited on Si wafer.

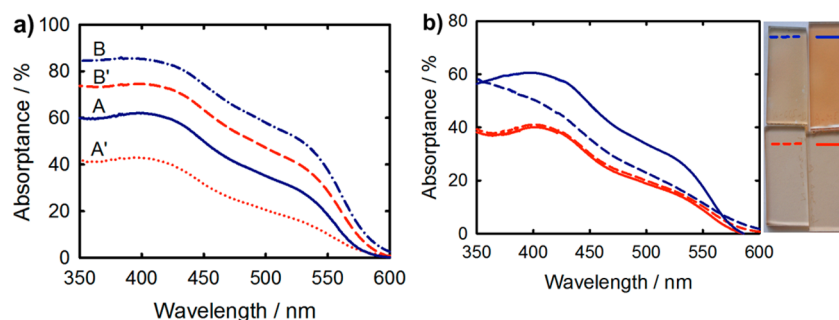


Figure 3. a) Absorbance spectra of ~ 18 nm hematite film with (curve A) and without (curve A') a Ga_2O_3 underlayer. B and B' curves correspond to a 60 nm films with and without a Ga_2O_3 underlayer, respectively. b) Absorbance spectra of ~ 18 nm hematite films with (dark blue) and without (red) a Ga_2O_3 underlayer before (dashed lines) and after (solid lines) annealing in 500°C .

possible effect of Ga doping, 300 ALD cycle hematite electrodes were doped with Ga by alternating ALD cycles of Fe_2O_3 and Ga_2O_3 and examined under water oxidation conditions. The extent of Ga doping was chosen to be the equivalent of 2 nm Ga_2O_3 , i.e. 18 ALD cycles (1 cycle of Ga_2O_3 after each 16 cycles of Fe_2O_3). Negligible photocurrent was observed for Ga doped hematite compared to the electrode with a Ga_2O_3 underlayer (Figure 3S). These combined results rule out any significant contribution from Ga doping.

Itoh and Bockris also suggested that when the hematite film is sufficiently thin, the diffusion length for electrons from the underlying SnO_2 substrate extends over a greater portion of the hematite film, causing enhanced electron–hole recombination.⁴³ Similar conclusion was made by Hisatomi et al., and it was suggested that this electron back recombination can be blocked by 2 nm of Nb_2O_5 or TiO_2 underlayers.⁴⁷ This electron-blocking effect is also possible for Ga_2O_3 , since its conduction band energy is more negative than that of hematite.⁵⁰ On the other hand, it is not trivial to define electronic bands for a material that is only 2 nm thick and highly mixed with adjacent SnO_2 and Fe_2O_3 layers. In any case, to address this possibility, we note that hematite is already highly doped, and bulk electron–hole recombination is generally limited by the rate of hole trapping.⁵² Therefore, increasing the number of electrons should have a negligible effect on the recombination rate. In addition, the electron blocking effect of a Ga_2O_3 underlayer should also improve the performance of Ti-doped electrodes; however, no additional improvement was observed for Ti-doped hematite electrode upon incorporation of the underlayer (Figure 1b). We therefore conclude that the underlayer does not improve the performance of thin film hematite electrodes by reducing recombination with FTO electrons.

Another cause of the performance improvement by the underlayer can simply be attributed to an increase in the concentration of photogenerated charge carriers due to an increase in the electrode thickness, e.g. increasing the growth rate of Fe_2O_3 , an increase in the absorptivity, α , or a reduction in the bandgap. To address these possibilities, absorption measurements were performed of films with and without a Ga_2O_3 underlayer. Figure 3a shows the absorbance spectra of ~ 18 and ~ 60 nm hematite films, with and without a Ga_2O_3 underlayer. No significant contribution in visible light absorption was observed for Ga_2O_3 as it is a wide band gap oxide and only 2 nm thick (Figure 4S). Surprisingly, the absorbance of the 18.9 nm film deposited on a Ga_2O_3 underlayer is significantly higher with more pronounced absorption peaks at ~ 530 and 400 nm. The absorption

spectrum and onset match quite well with the unmodified hematite film, however, indicating no changes in the hematite band gap or major electronic transitions by the Ga_2O_3 underlayer as expected. A larger absorbance was also observed for ~ 60 nm films with a Ga_2O_3 underlayer; however, the extent of the absorbance increase was lower compared to 18.9 nm films. Thus, at least part of the improved performance of hematite electrodes with a Ga_2O_3 underlayer can be attributed to increased light absorption. The increased light absorption must be due to an increased hematite film thickness and/or increased absorptivity. A plot of the absorbance spectra of ~ 18 nm electrodes with and without a Ga_2O_3 underlayer is shown in Figure 5S. The absorbance at 550 nm is 0.202 and 0.105 for the films with and without a Ga_2O_3 underlayer, respectively. Assuming the same absorption coefficient of $8 \times 10^4 \text{ cm}^{-1}$ at this wavelength,⁵ the thickness of the film with the underlayer is about double of that without the underlayer. Therefore, if the increased absorption is simply due to an increased thickness, it should be clearly observable by ellipsometry as well as from the XPS depth profiles. The thickness of the 300 ALD cycle hematite film deposited on bare and Ga_2O_3 coated FTO were measured directly by ellipsometry, and it was found to be the same within experimental error. The relative thicknesses were also compared from XPS depth profiling measurements of films containing 400 ALD cycles hematite grown on Si wafers with and without a Ga_2O_3 underlayer. Similar profiles of Fe were observed in both cases which indicates that the thicknesses of Fe_2O_3 are nominally the same (Figure 6S). Any small difference in thickness, within experimental error of this measurement, cannot account for the large difference in the film absorbances. Thus, the increased light absorption is due to an increased absorptivity.

Interestingly, we noticed that the color of the hematite electrodes deposited on Ga_2O_3 underlayers turn a darker orange during thermal annealing (see the inset of Figure 3b); however, the hematite films deposited directly on FTO did not. Absorption measurements of hematite films were therefore carried out for hematite films with and without Ga_2O_3 underlayer films both before and after annealing at 500°C . The absorbance spectra of ~ 18 nm hematite film deposited on bare and Ga_2O_3 coated FTO are shown in Figure 3b. Interestingly, the higher absorbance and clear absorption peaks only appear after annealing for the films with a Ga_2O_3 underlayer. We note that crystalline hematite ($\alpha\text{-Fe}_2\text{O}_3$) generally forms after annealing at temperatures $\sim 500^\circ\text{C}$ or higher.¹⁴ Below this temperature, amorphous Fe_2O_3 is the dominant component of films prepared via ALD. This is consistent with the spectral profile of the unannealed films

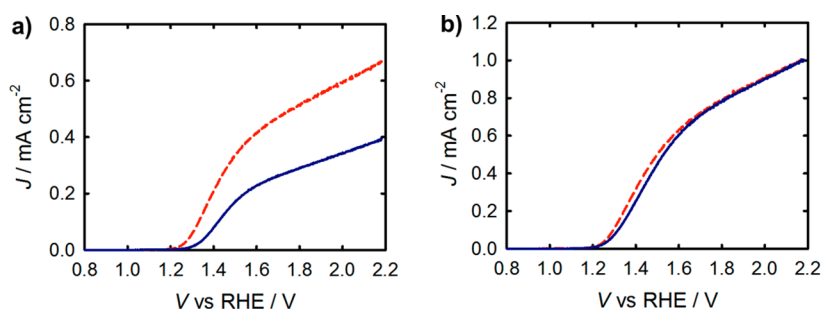
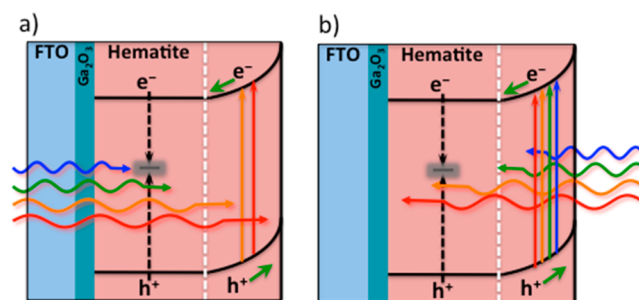


Figure 4. J – V curves of ~ 60 nm hematite electrodes with (solid dark blue) and without (dashed red) a Ga_2O_3 underlayer. a) Back side (substrate side) illumination. b) Front side (electrolyte side) illumination.

which clearly show characteristics of an amorphous phase, with no well-defined transition peaks. After annealing, however, the absorption onset and electronic transition responsible for indirect and direct transitions of hematite can be clearly distinguished at ~ 530 and 400 nm, respectively.^{51,52} The absorbance of the unannealed film with the underlayer was slightly higher than the films without an underlayer which we attribute to the different scattering properties of the hematite film in the presence of a Ga_2O_3 underlayer (see below). Similar absorption properties were observed for ~ 18 nm hematite films with an Nb_2O_5 underlayer under similar conditions (Figure 7S). A higher absorptivity was also observed for hematite films annealed at elevated temperatures by Pailhé et al. which was attributed to the larger crystallite size. They suggested that larger crystallite size allows for structural relaxation from octahedral to C_{3v} like symmetry, which in turn alters the optical transition properties manifested as increased absorptivity of the films.⁵³ The correlation between the size of the crystallites and absorptivity was also observed by Sivula et al. for mesoporous hematite films annealed at various temperatures.⁵⁴ Therefore, the increased absorptivity for the hematite films with a Ga_2O_3 underlayer which correlates with the larger crystallite size (see below) is attributed to the same effect.

Figure 4a shows J – V curves of ~ 60 nm hematite electrodes with and without a Ga_2O_3 underlayer. The Ga_2O_3 underlayer did not improve the water oxidation performance of thicker hematite electrodes but also resulted in a significant loss in the plateau photocurrent. We note that lower photocurrent at higher hematite thicknesses with an oxide underlayer was also observed by Hisatomi and co-workers who attributed it to a lower electron extraction efficiency as a result of the electron-blocking effect of the oxide underlayer.⁴⁸ The lower photocurrent of the thick electrodes on a Ga_2O_3 underlayer can also be accounted for by the higher absorbance of these films; since more light is absorbed near the substrate, fewer holes are generated in the depletion region near the electrolyte interface. We have previously determined that holes generated outside of the ~ 20 nm depletion region undergo recombination and do not contribute to the water oxidation photocurrent (i.e., the diffusion length is essentially zero).¹⁴ If a stronger absorbance is the cause of the lower plateau photocurrent of the 60 nm films, illuminating the electrodes for the front side (electrolyte side) should overcome this and produce an essentially identical J – V response. These situations are illustrated in Scheme 1. Figure 4b shows the J – V curves of the front illuminated 60 nm electrodes with and without a Ga_2O_3 underlayer, which are nominally identical. This confirms our assignment of the Ga_2O_3 underlayer effect of primarily increasing the absorptivity of hematite thin films. This effect should result in the spectral

Scheme 1. Schematic Electronic Transitions of ~ 60 nm Hematite Electrodes under Back Side (a) and Front Side (b) Illumination Directions^a



^aNote that the short wavelengths do not contribute much to the photocurrent when illuminated from the backside.

response due to differences in light penetration depths. The incident photocurrent efficiency (IPCE) measurements (Figure 8S) clearly show that the shorter wavelengths contribute less to the photocurrent when illuminated from the substrate side compared to the electrolyte side. The redder wavelengths, which have a longer penetration depth, are only minimally affected by the illumination direction. These combined results confirm our assignment of increased absorptivity as a significant effect of the underlayer.

In addition to an increased absorptivity, inspection of Figure 3b indicates that the absorption peaks at ~ 530 and 400 nm of the hematite film with an underlayer are somewhat more prominent. These observations are consistent with a more ordered structure and atomic arrangement, i.e. an increased crystallinity of the films deposited on Ga_2O_3 as others have suggested.⁴⁶ A common method to measure the degree of crystallinity and confirm this assignment is X-ray diffraction, XRD. In the case of the ultrathin films of interest herein, however, it is not feasible to resolve the hematite peaks from underlying FTO substrate signal by conventional XRD. Raman spectroscopy, however, is a more surface sensitive technique that has been utilized extensively to investigate amorphous to crystalline phase transitions, oxygen defects, stress states, and quantum size effects in metal oxides.^{55–60} Raman spectra provide not only the basic structural information but also subtle spectra alterations, such as the line shape and full width at half-maximum (fwhm) of Raman peaks, and can be used to access crystalline quality of nanostructures.^{55,60–62} Crystalline quality can be described in terms of correlation length, which is defined as the average size of the material homogeneity region corresponding to the actual grain size, average distance between defects, or grain boundaries. So-called phonon confinement

(PC) effects are often used to explain the correlation length and quality of the crystalline medium.^{55,57,60} PC effects describe the phenomena that occur when the phonon momentum selection rule is deviated. This generally happens when the dimension of ordered crystal domains become very small and manifests as both frequency shift and asymmetrical broadening of the Raman bands.^{55,57,60} We therefore employed Raman spectroscopy to examine the degree of crystallinity in the thin films of interest here.

A Raman spectrum of a ~ 60 nm hematite film deposited on FTO is shown in Figure 9S overlaid with the spectra for bare FTO. The Raman spectrum of hematite is distinct from that of other iron oxide phases.^{57,58,61,63,64} Seven Raman bands at 222, 239, 286, 403, 488, 600, and 1300 cm^{-1} can be clearly resolved, which match quite well with the reported values for hematite in the literature and that of a reference hematite sample.^{57,58,61} Figure 5 shows four major Raman phonon modes of ~ 18 nm

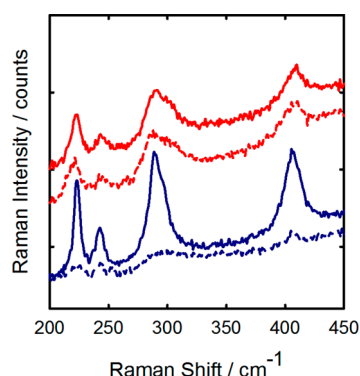


Figure 5. Raman spectra of four major hematite phonon modes of 18 nm hematite films with (dark blue) and without (red) a Ga_2O_3 underlayer before (dashed lines) and after (solid lines) annealing. The fwhm for the peak at 288 cm^{-1} is 12.40 and 27.97 cm^{-1} for the films with and without a Ga_2O_3 underlayer, respectively.

hematite films with and without a Ga_2O_3 underlayer. Interestingly, the trend of the Raman spectra match the absorption spectra; more intense and sharper Raman peaks were observed in the films with a Ga_2O_3 underlayer but only after annealing. Annealing had a negligible effect on the Raman spectra for the films without an underlayer. The fwhm for the peak at 288 cm^{-1} was found to be 12.40 and 27.97 cm^{-1} for the annealed films with and without the Ga_2O_3 underlayer, respectively. The asymmetric broadening along with a subtle blue shift of the peaks was observed for the hematite film without an underlayer. Peak broadening and frequency shifts have been extensively observed for TiO_2 nanocrystals and

hematite thin films which have been attributed to phonon confinement, internal stress, and nonstoichiometry.^{55,58,61} In our films, since the preparation condition was strictly the same for an electrode with and without an underlayer, the effects of impurities and nonstoichiometry are unlikely which we rule out. Therefore, we attribute the peak shift and broadening to the lower crystallinity and smaller crystallite size for hematite films deposited on bare FTO. To confirm this assignment, high resolution SEM images were taken for ~ 18 nm hematite films deposited on bare FTO and on a Ga_2O_3 underlayer as shown in Figure 6. Thin films of hematite deposited on a Ga_2O_3 underlayer exhibit significantly larger grain sizes along with a more ordered structure compared to the film without the underlayer. An additional SEM image of a hematite film with an Nb_2O_5 underlayer is shown in Figure 10S. Further, we note that this assignment is consistent with the absorption spectra in Figure 3, i.e. more pronounced peaks and increased absorptivity correlates with the larger grain size for hematite films deposited on a Ga_2O_3 underlayer as observed by others.^{53,54}

Another interesting comparison is the effect of different oxide underlayers which have been reported to improve the water oxidation performance of hematite thin films.^{20,47} Figure 7a shows the Raman spectra of ~ 18 nm hematite films deposited on bare FTO and three different oxide underlayers including Ga_2O_3 , Nb_2O_5 , and WO_3 , as well as an ITO-coated glass substrate. The J - V curves of hematite films deposited on each of these underlayers, and directly on FTO, are shown in Figure 7b. Clearly all of the oxide underlayers improve the water oxidation performance, however, to different extents. Interestingly the intensity and sharpness of the Raman bands can be correlated to the improvement in the photocatalytic activity of the corresponding electrodes. The effect of the ITO and WO_3 underlayers on the J - V curves is less dramatic compared to the Ga_2O_3 and Nb_2O_5 underlayers. The Raman spectra of the films with WO_3 or ITO also show a subtle broadening and peak shift compared to the corresponding films with either Ga_2O_3 or Nb_2O_5 underlayers. In addition, each of these underlayers produced an enhanced absorbance, with the spectra shown in Figure 7c. The fwhm extracted from the Raman spectra (See Figure 12S) indicate a strong general correlation between the Raman line shapes, absorptivity, and photocatalytic activity. These results are all consistent with our assignment of increased crystallinity as being the primary beneficial effect of a metal oxide underlayer.

CONCLUSION

A combination of photoelectrochemical, spectroscopic, and SEM measurements presented herein shed light on the origin

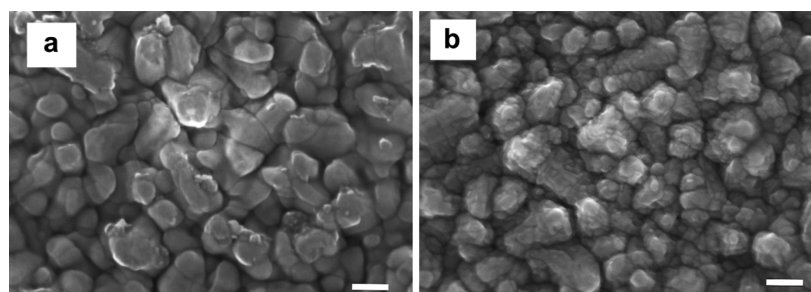


Figure 6. SEM images of ~ 18 nm hematite on FTO with (a) and without (b) a Ga_2O_3 underlayer. The scale bar is 100 nm for both images. Additional images are provided in the SI.

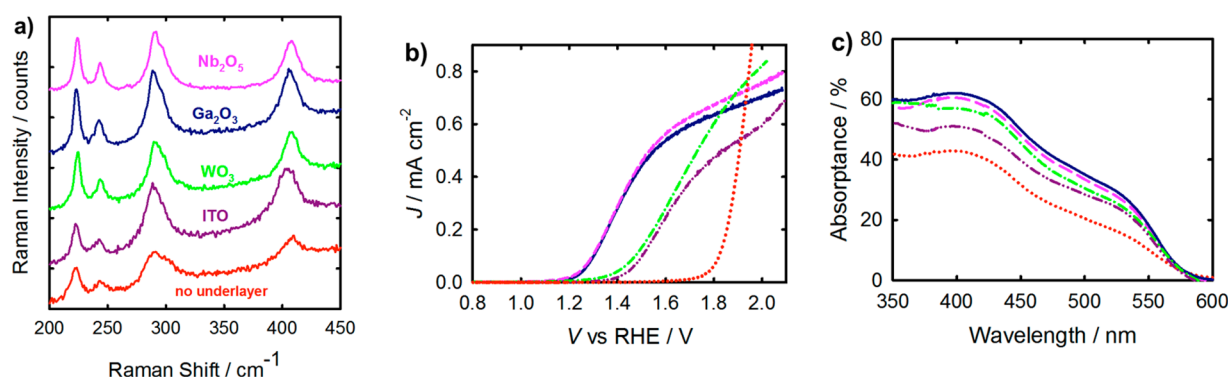


Figure 7. a) Raman spectra of ~ 18 nm hematite films on FTO and on different 2 nm thick oxide underlayers. The fwhm for the peaks at 288 cm^{-1} are 12.20, 12.40, 14.30, and 15.15 cm^{-1} for the films with a Nb_2O_5 , Ga_2O_3 , WO_3 , or ITO underlayer, respectively, and 27.97 cm^{-1} without an underlayer. b) J - V curves of the same films shown in a) under 1 sun illumination. c) Absorbance spectra of the same films shown in a).

of the poor water oxidation performance of very thin hematite films, the origin of the dead layer, and the effect of metal oxide underlayers. The hematite films deposited on bare FTO exhibit poor crystallinity with small crystallite domains. This could result in a high density of defects and grain boundaries, which may increase the rate of recombination near the back contact. An amorphous, or low crystallinity, region at the interface would also diminish the already low mobility of minority carriers which would prevent efficient charge transport. The effects of increased recombination and decreased mobility for the very thin films that are relevant here are difficult to separate; however, we note that both effects are likely and would greatly diminish the water splitting performance. Once the thickness of the hematite films increases beyond the dead layer region, with a critical thickness ~ 20 nm, the film crystallinity increases which results in an improved water oxidation performance, as discussed above for ~ 60 nm films. In order to realize the host-guest strategy of making nano-structured electrodes, it is optimal to only make electrodes as thick as the collection length. Thus, it is crucial to not only understand the limitations of very thin electrodes but also to establish methods to overcome them. We demonstrated that Ga_2O_3 and Nb_2O_5 are promising oxide underlayers that enable the deposition of highly crystalline hematite films with the average crystallite size of ~ 3 times larger than that of the films deposited on bare FTO according to SEM images. The increased crystallinity manifests as an increased correlation length of the crystalline medium, which results in the sharper Raman peaks. In addition, the increased crystallinity results in stronger light absorbance with more defined transition peaks. It is further expected that such an increased crystallinity would improve the hole mobility which would result in a higher charge collection efficiency; we cannot rule out the possibility of a concomitant decrease in the rate of recombination near the FTO interface.

Surprisingly, the effect of the underlayer appears to be similar to that of the Ti doping—to the same extent and with higher enhancement observed for the thinnest electrodes. A similar result was also observed by Liang et al. for hematite thin films upon incorporation of the SnO_2 underlayer or Si doping.⁴⁴ The strong agreement between doping and underlayers indicate that the improved water oxidation performance may arise from similar effects, namely increased crystallinity. The chemical cause of the increased crystallinity induced by incorporating a high concentration of Ti dopant atoms compared to a Ga_2O_3 underlayer is very likely to be distinct; however, this has not yet

been elucidated and is the subject of ongoing efforts on our laboratory.

■ ASSOCIATED CONTENT

● Supporting Information

Plots of dark J - V curves, J - V curves measured for different Ga_2O_3 underlayer thickness and doped samples, transmittance and absorbance spectra, depth profiling results, IPCE and Raman plots of 60 nm hematite films, SEM images, and fit results of Raman peaks of different underlayer materials. This material is available free of charge via the Internet at <http://pubs.acs.org>.

■ AUTHOR INFORMATION

Corresponding Author

*E-mail: hamann@chemistry.msu.edu.

Notes

The authors declare no competing financial interest.

■ ACKNOWLEDGMENTS

T.W.H. is grateful to the National Science Foundation (CHE-1150378) for support of this research. XPS was performed at the Molecular Materials Research Center in the Beckman Institute at the California Institute of Technology.

■ REFERENCES

- (1) Grätzel, M. Photoelectrochemical Cells. *Nature* **2001**, *414*, 338.
- (2) Walter, M. G.; Warren, E. L.; McKone, J. R.; Boettcher, S. W.; Mi, Q.; Santori, E. A.; Lewis, N. S. Solar Water Splitting Cells. *Chem. Rev.* **2010**, *110*, 6446–6473.
- (3) Lewis, N. S.; Nocera, D. G. Powering the Planet: Chemical Challenges in Solar Energy Utilization. *Proc. Natl. Acad. Sci. U. S. A.* **2006**, *103*, 15729–15735.
- (4) Klahr, B.; Gimenez, S.; Fabregat-Santiago, F.; Hamann, T.; Bisquert, J. Water Oxidation at Hematite Photoelectrodes: The Role of Surface States. *J. Am. Chem. Soc.* **2012**, *134*, 4294–4302.
- (5) Young, K. M. H.; Klahr, B. M.; Zandi, O.; Hamann, T. W. Photocatalytic Water Oxidation with Hematite Electrodes. *Catal. Sci. Technol.* **2013**, *3*, 1660–1671.
- (6) Fijishima, A.; Honda, K. Electrochemical Photolysis of Water at a Semiconductor Electrode. *Nature* **1972**, *238*, 37–38.
- (7) Chen, Z.; Jaramillo, T. F.; Deutsch, T. G.; Kleiman-Shwarscstein, A.; Forman, A. J.; Gaillard, N.; Garland, R.; Takanabe, K.; Heske, C.; Sunkara, M.; et al. Accelerating Materials Development for Photoelectrochemical Hydrogen Production: Standards for Methods, Definitions, and Reporting Protocols. *J. Mater. Res.* **2011**, *25*, 3–16.

- (8) Li, Z.; Luo, W.; Zhang, M.; Feng, J.; Zou, Z. Photoelectrochemical Cells for Solar Hydrogen Production: Current State of Promising Photoelectrodes, Methods to Improve Their Properties, and Outlook. *Energy Environ. Sci.* **2013**, *6*, 347–370.
- (9) Sivula, K.; Le Formal, F.; Grätzel, M. Solar Water Splitting: Progress Using Hematite ($\alpha\text{-Fe}_2\text{O}_3$) Photoelectrodes. *ChemSusChem* **2011**, *4*, 432–449.
- (10) Hamann, T. W. Splitting Water with Rust: Hematite Photoelectrochemistry. *Dalton Trans.* **2012**, *41*, 7830–7834.
- (11) Itoh, K.; Bockris, J. O. Stacked Thin-Film Photoelectrode Using Iron Oxide. *J. Appl. Phys.* **1984**, *56*, 874.
- (12) Kay, A.; Cesar, I.; Grätzel, M. New Benchmark for Water Photooxidation by Nanostructured $\alpha\text{-Fe}_2\text{O}_3$ Films. *J. Am. Chem. Soc.* **2006**, *128*, 15714–15721.
- (13) Katz, M. J.; Riha, S. C.; Jeong, N. C.; Martinson, A. B. F.; Farha, O. K.; Hupp, J. T. Toward Solar Fuels: Water Splitting with Sunlight and “Rust”? *Coord. Chem. Rev.* **2012**, *256*, 2521–2529.
- (14) Klahr, B. M.; Martinson, A. B. F.; Hamann, T. W. Photoelectrochemical Investigation of Ultrathin Film Iron Oxide Solar Cells Prepared by Atomic Layer Deposition. *Langmuir* **2011**, *27*, 461–468.
- (15) Cesar, I.; Kay, A.; Gonzalez Martinez, J. A.; Grätzel, M. Translucent Thin Film Fe_2O_3 Photoanodes for Efficient Water Splitting by Sunlight: Nanostructure-Directing Effect of Si-Doping. *J. Am. Chem. Soc.* **2006**, *128*, 4582–4583.
- (16) Lin, Y.; Zhou, S.; Sheehan, S. W.; Wang, D. Nanonet-Based Hematite Heteronanostructures for Efficient Solar Water Splitting. *J. Am. Chem. Soc.* **2011**, *133*, 2398–2401.
- (17) Riha, S. C.; Devries Vermeer, M. J.; Pellin, M. J.; Hupp, J. T.; Martinson, A. B. F. Hematite-Based Photo-Oxidation of Water Using Transparent Distributed Current Collectors. *ACS Appl. Mater. Interfaces* **2013**, *5*, 360–367.
- (18) Wheeler, D. A.; Wang, G.; Ling, Y.; Li, Y.; Zhang, J. Z. Nanostructured Hematite: Synthesis, Characterization, Charge Carrier Dynamics, and Photoelectrochemical Properties. *Energy Environ. Sci.* **2012**, *5*, 6682.
- (19) Tilley, S. D.; Cornuz, M.; Sivula, K.; Grätzel, M. Light-Induced Water Splitting with Hematite: Improved Nanostructure and Iridium Oxide Catalysis. *Angew. Chem., Int. Ed. Engl.* **2010**, *49*, 6405–6408.
- (20) Sivula, K.; Formal, F. Le; Grätzel, M. $\text{WO}_3\text{-Fe}_2\text{O}_3$ Photoanodes for Water Splitting: A Host Scaffold, Guest Absorber Approach. *Chem. Mater.* **2009**, *21*, 2862–2867.
- (21) Stefik, M.; Cornuz, M.; Mathews, N.; Hisatomi, T.; Mhaisalkar, S.; Grätzel, M. Transparent, Conducting Nb:SnO_2 for Host-Guest Photoelectrochemistry. *Nano Lett.* **2012**, *12*, 5431–5435.
- (22) Klahr, B. M.; Hamann, T. W. Voltage Dependent Photocurrent of Thin Film Hematite Electrodes. *Appl. Phys. Lett.* **2011**, *99*, 063508.
- (23) Klahr, B.; Gimenez, S.; Fabregat-Santiago, F.; Bisquert, J.; Hamann, T. W. Electrochemical and Photoelectrochemical Investigation of Water Oxidation with Hematite Electrodes. *Energy Environ. Sci.* **2012**, *5*, 7626.
- (24) Peter, L. M.; Wijayantha, K. G. U.; Tahir, A. A. Kinetics of Light-Driven Oxygen Evolution at $\alpha\text{-Fe}_2\text{O}_3$ Electrodes. *Faraday Discuss.* **2012**, *155*, 309.
- (25) Cummings, C. Y.; Marken, F.; Peter, L. M.; Tahir, A. A.; Wijayantha, K. G. U. Kinetics and Mechanism of Light-Driven Oxygen Evolution at Thin Film $\alpha\text{-Fe}_2\text{O}_3$ Electrodes. *Chem. Commun.* **2012**, *48*, 2027–2029.
- (26) Barroso, M.; Pendlebury, S.; Cowan, A.; Durrant, J. Charge Carrier Trapping, Recombination and Transfer in Hematite ($\alpha\text{-Fe}_2\text{O}_3$) Water Splitting Photoanodes. *Chem. Sci.* **2013**, *4*, 2724.
- (27) Zhong, D. K.; Cornuz, M.; Sivula, K.; Grätzel, M.; Gamelin, D. R. Photo-Assisted Electrodeposition of Cobalt–phosphate (Co–Pi) Catalyst on Hematite Photoanodes for Solar Water Oxidation. *Energy Environ. Sci.* **2011**, *4*, 1759.
- (28) Barroso, M.; Mesa, C. A.; Pendlebury, S. R.; Cowan, A. J.; Hisatomi, T.; Sivula, K.; Grätzel, M.; Klug, D. R.; Durrant, J. R. Dynamics of Photogenerated Holes in Surface Modified $\alpha\text{-Fe}_2\text{O}_3$ Photoanodes for Solar Water Splitting. *Proc. Natl. Acad. Sci. U. S. A.* **2012**, *109*, 15640–15645.
- (29) Klahr, B.; Gimenez, S.; Fabregat-Santiago, F.; Bisquert, J.; Hamann, T. W. Photoelectrochemical and Impedance Spectroscopic Investigation of Water Oxidation with “Co–Pi”-Coated Hematite Electrodes. *J. Am. Chem. Soc.* **2012**, *134*, 16693–16700.
- (30) Liao, P.; Toroker, M. C.; Carter, E. A. Electron Transport in Pure and Doped Hematite. *Nano Lett.* **2011**, *11*, 1775–1781.
- (31) Zandi, O.; Klahr, B.; Hamann, T. Highly Photoactive Ti-Doped $\text{A-Fe}_2\text{O}_3$ Thin Film Electrodes; Resurrection of the Dead Layer. *Energy Environ. Sci.* **2012**, *6*, 634–642.
- (32) Glasscock, J. A.; Barnes, P. R. F.; Plumb, I. C.; Savvides, N. Enhancement of Photoelectrochemical Hydrogen Production from Hematite Thin Films by the Introduction of Ti and Si. *J. Phys. Chem. C* **2007**, *111*, 16477–16488.
- (33) Cesar, I.; Sivula, K.; Kay, A. Influence of Feature Size, Film Thickness, and Silicon Doping on the Performance of Nanostructured Hematite Photoanodes for Solar Water Splitting. *J. Phys. Chem. C* **2009**, *113*, 772–782.
- (34) Ling, Y.; Wang, G.; Wheeler, D. A.; Zhang, J. Z.; Li, Y. Sn-doped Hematite Nanostructures for Photoelectrochemical Water Splitting. *Nano Lett.* **2011**, *11*, 2119–2125.
- (35) Wang, G.; Ling, Y.; Wheeler, D. A.; George, K. E. N.; Horsley, K.; Heske, C.; Zhang, J. Z.; Li, Y. Facile Synthesis of Highly Photoactive $\alpha\text{-Fe}_2\text{O}_3$ -Based Films for Water Oxidation. *Nano Lett.* **2011**, *11*, 3503–3509.
- (36) Photoanodes, O.; Hahn, N. T.; Mullins, C. B. Photoelectrochemical Performance of Nanostructured Ti- and Sn-doped. *Chem. Mater.* **2010**, *22*, 6474–6482.
- (37) Hu, Y.-S.; Kleiman-Shwarsstein, A.; Stucky, G. D.; McFarland, E. W. Improved Photoelectrochemical Performance of Ti-Doped $\alpha\text{-Fe}_2\text{O}_3$ Thin Films by Surface Modification with Fluoride. *Chem. Commun.* **2009**, 2652–2654.
- (38) Hu, Y.; Kleiman-Shwarsstein, A.; Forman, A. J.; Hazen, D.; Park, J.; McFarland, E. W.; Barbara, S. Pt-doped $\alpha\text{-Fe}_2\text{O}_3$ Thin Films Active for Photoelectrochemical Water Splitting. *Chem. Mater.* **2008**, *20*, 3803–3805.
- (39) Kleiman-Shwarsstein, A.; Hu, Y.-S.; Forman, A. J.; Stucky, G. D.; McFarland, E. W. Electrodeposition of $\alpha\text{-Fe}_2\text{O}_3$ Doped with Mo or Cr as Photoanodes for Photocatalytic Water Splitting. *J. Phys. Chem. C* **2008**, *112*, 15900–15907.
- (40) Sanchez, H. L.; Steinfink, H.; White, H. S. Solid Solubility of Ge, Si, and Mg in Fe_2O_3 and Photoelectric Behavior. *J. Solid State Chem.* **1982**, *41*, 90–96.
- (41) Sanchez, C.; Sieber, K. D.; Somorjai, G. A. The Photoelectrochemistry of Niobium Doped $\alpha\text{-Fe}_2\text{O}_3$. *J. Electroanal. Chem. Interfacial Electrochem.* **1988**, *252*, 269–290.
- (42) Le Formal, F.; Grätzel, M.; Sivula, K. Controlling Photoactivity in Ultrathin Hematite Films for Solar Water-Splitting. *Adv. Funct. Mater.* **2010**, *20*, 1099–1107.
- (43) Itoh, K. Thin Film Photoelectrochemistry: Iron Oxide. *J. Electrochem. Soc.* **1984**, *131*, 1266.
- (44) Liang, Y.; Enache, C. S.; van de Krol, R. Photoelectrochemical Characterization of Sprayed $\text{A-Fe}_2\text{O}_3$ Thin Films: Influence of Si Doping and SnO_2 Interfacial Layer. *Int. J. Photoenergy* **2008**, *2008*, 1–7.
- (45) Souza, F. L.; Lopes, K. P.; Longo, E.; Leite, E. R. The Influence of the Film Thickness of Nanostructured $\alpha\text{-Fe}_2\text{O}_3$ on Water Photooxidation. *Phys. Chem. Chem. Phys.* **2009**, *11*, 1215–1219.
- (46) Hisatomi, T.; Brillet, J.; Cornuz, M.; Le Formal, F.; Tétreault, N.; Sivula, K.; Grätzel, M. A Ga_2O_3 Underlayer as an Isomorphic Template for Ultrathin Hematite Films Toward Efficient Photoelectrochemical Water Splitting. *Faraday Discuss.* **2012**, *155*, 223.
- (47) Hisatomi, T.; Dotan, H.; Stefik, M.; Sivula, K.; Rothschild, A.; Grätzel, M.; Mathews, N. Enhancement in the Performance of Ultrathin Hematite Photoanode for Water Splitting by an Oxide Underlayer. *Adv. Mater.* **2012**, *24*, 2699–2702.

- (48) Dezelah, C. L.; Niinisto, J.; Arstila, K.; Niinisto, L.; Winter, C. H. Atomic Layer Deposition of Ga_2O_3 Films from a Dialkylamido-Based Precursor. *Chem. Mater.* **2006**, *18*, 471–475.
- (49) Kronawitter, C. X.; Zegkinoglou, I.; Rogero, C.; Guo, J.-H.; Mao, S. S.; Himpsel, F. J.; Vayssieres, L. On the Interfacial Electronic Structure Origin of Efficiency Enhancement in Hematite Photoanodes. *J. Phys. Chem. C* **2012**, *116*, 22780–22785.
- (50) Xu, Y.; Schoonen, M. The Absolute Energy Positions of Conduction and Valence Bands of Selected Semiconducting Minerals. *Am. Mineral.* **2000**, *85*, 543–556.
- (51) Sherman, D. M.; Waite, D. T. Electronic Spectra of Fe^{3+} Oxides and Oxide Hydroxides in the Near IR to Near UV. *Am. Mineral.* **2000**, *70*, 1262–1269.
- (52) Marusai, L. A.; Messier, R.; White, W. B. Optical Absorption Spectrum of Hematite, $\alpha\text{-Fe}_2\text{O}_3$ Near IR to UV. *J. Phys. Chem. Solids* **1980**, *41*, 981–984.
- (53) Pailhé, N.; Wattiaux, A.; Gaudon, M.; Demourgues, A. Impact of Structural Features on Pigment Properties of $\alpha\text{-Fe}_2\text{O}_3$ Haematite. *J. Solid State Chem.* **2008**, *181*, 2697–2704.
- (54) Sivula, K.; Zboril, R.; Le Formal, F.; Robert, R.; Weidenkaff, A.; Tucek, J.; Frydrych, J.; Grätzel, M. Photoelectrochemical Water Splitting with Mesoporous Hematite Prepared by a Solution-Based Colloidal Approach. *J. Am. Chem. Soc.* **2010**, *132*, 7436–7444.
- (55) Bersani, D.; Lottici, P. P.; Ding, X.-Z. Phonon Confinement Effects in the Raman Scattering by TiO_2 Nanocrystals. *Appl. Phys. Lett.* **1998**, *72*, 73.
- (56) Bersani, D. Micro-Raman Investigation of Iron Oxide Films and Powders Produced by Sol–gel Syntheses. *J. Raman Spectrosc.* **1999**, *30*, 355–360.
- (57) de Faria, D. Raman Microspectroscopy of Some Iron Oxides and Oxyhydroxides. *J. Raman Spectrosc.* **1997**, *28*, 873–878.
- (58) Jubb, A. M.; Allen, H. C. Vibrational Spectroscopic Characterization of Hematite, Maghemite, and Magnetite Thin Films Produced by Vapor Deposition. *ACS Appl. Mater. Interfaces* **2010**, *2*, 2804–2812.
- (59) Heutz, S.; Salvan, G.; Silaghi, S. Raman Scattering as a Probe of Crystallinity in PTCDA and H_2Pc Single-Layer and Double-Layer Thin Film Heterostructures. *J. Phys. Chem. B* **2003**, *107*, 3782–3788.
- (60) Balaji, S.; Djaoued, Y.; Robichaud, J. Phonon Confinement Studies in Nanocrystalline anatase- TiO_2 Thin Films by Micro Raman Spectroscopy. *J. Raman Spectrosc.* **2006**, *37*, 1416–1422.
- (61) Chernyshova, I. V.; Hochella, M. F.; Madden, A. S. Size-Dependent Structural Transformations of Hematite Nanoparticles. 1. Phase Transition. *Phys. Chem. Chem. Phys.* **2007**, *9*, 1736–1750.
- (62) Xu, Y. Y.; Zhao, D.; Zhang, X. J.; Jin, W. T.; Kashkarov, P.; Zhang, H. Synthesis and Characterization of Single-Crystalline $\alpha\text{-Fe}_2\text{O}_3$ Nanoleaves. *Phys. E (Amsterdam, Neth.)* **2009**, *41*, 806–811.
- (63) Onari, S.; Arai, T.; Kudo, K. Infrared Lattice Vibrations and Dielectric Dispersion in $\alpha\text{-Fe}_2\text{O}_3$. *Phys. Rev. B* **2008**, *16*, 1717–1721.
- (64) Glasscock, J. A.; Barnes, P. R. F.; Plumb, I. C.; Bendavid, A.; Martin, P. J. Structural, Optical and Electrical Properties of Undoped Polycrystalline Hematite Thin Films Produced Using Filtered Arc Deposition. *Thin Solid Films* **2008**, *516*, 1716–1724.